https://doi.org/10.5194/egusphere-2026-5242
Preprint. Discussion started: 14 September 2026

Seasonal and local-time patterns of VTEC and dTEC RMS over Hainan: temporal and horizontal characteristics of winter and summer enhancements

Zheng Wang[1,2,3], Yusen Tian[1,4], Guangwei Cao[1,4], Guojun Wang[1,2,3], Guangyuan Tan[1,4], Kai Ding[1,2], Yajun Zhu[1,2,3], and Xiao Wang[1,2,3]

[1] National Space Science Center, Chinese Academy of Sciences, Beijing, China
[2] State Key Laboratory of Solar Activity and Space Weather, Beijing, China
[3] National Field Observation and Research Station (Hainan) for Space Weather, Hainan, China
[4] Beijing Key Laboratory of Space Environment Exploration, Beijing 100190, China

Correspondence: Zheng Wang (zwang@swl.ac.cn)

Abstract. Background vertical total electron content (VTEC) and short-timescale TEC variability describe different aspects of the low-latitude ionosphere. Previous East Asian studies established winter daytime and warm-season nighttime disturbances, but it remained unclear whether the winter and summer enhancements have the same temporal and horizontal character. We analyzed daily-balanced GPS and BeiDou observations from 1,793 dates during 2015-2020 over Hainan. VTEC followed daytime plasma buildup and was strongest in autumn, with a later afternoon maximum in midsummer. Detrended TEC root-mean-square amplitude (dTEC RMS) instead peaked in winter afternoons and shifted toward late evening and midnight during spring and summer. We then compared BeiDou paths that remained near one ionospheric location with paths that crossed the surrounding region. In winter, both types showed the afternoon enhancement, including within comparable viewing directions. The winter structures therefore evolve over or pass through Hainan; a stationary horizontal gradient alone cannot explain the climatological maximum. In summer, the near-midnight enhancement was also present at nearly fixed locations, confirming a temporal increase, but its strength changed markedly among viewing directions and sampled regions. The summer structures are therefore more likely concentrated in particular regions or directions than spread uniformly across the Hainan sector. Spring and autumn show the orderly transition between these winter-afternoon and warm-season near-midnight environments. Together, the results show that winter and summer dTEC enhancements share temporal development but differ in their horizontal distribution.

1 Introduction

At low latitudes, vertical total electron content (VTEC) is shaped by solar production and loss, neutral winds, and electrodynamic transport within the equatorial ionization anomaly (EIA). These processes produce a strong daily cycle and marked seasonal and longitudinal differences (Balan et al., 2018; Zhao et al., 2009). Satellite observations and global ionospheric maps further show that EIA crest positions vary with longitude, solar activity, season, and local time (Nigussie et al., 2022; Dunn et al., 2024). Measurements from southern China have long shown a pre-dawn minimum, a post-noon maximum, and seasonal changes in both the size and timing of that maximum (Wu et al., 2012).

The amount of plasma and the strength of short-timescale structure are related but different properties. A high-VTEC ionosphere can be smooth, while waves, gradients, or irregularity boundaries can produce strong changes when the background content is moderate or low. Satellite-specific detrended TEC therefore adds information that is not contained in the VTEC daily cycle alone. Nearly fixed and moving ionospheric pierce points provide a further physical comparison: a nearly fixed path emphasizes change with time at one location, whereas a moving path also crosses horizontal structure (Huang et al., 2018; Bolmgren et al., 2020; Luo et al., 2024).

Two-dimensional TEC perturbation maps made the spatial evolution of traveling ionospheric disturbances visible over dense receiver networks (Saito et al., 1998; Tsugawa et al., 2007). Subsequent climatologies summarized selected MSTID events by season, local time, latitude, longitude, and solar activity (Kotake et al., 2006; Otsuka et al., 2021). More recent East Asian studies used fixed BeiDou GEO paths, dense GNSS networks, Fourier analysis, and automatic classification to establish winter daytime disturbances and warm-season nighttime populations (Hu et al., 2021; Cheng et al., 2021; Le et al., 2024; Li et al., 2024). These approaches identify recognizable events and quantify their occurrence or propagation. The present analysis measures dTEC amplitude across all eligible observations, including weaker or unclassified structure.

Amplitude climatologies provide a broader view than event occurrence alone. Zhang et al. (2026) mapped absolute and relative irregularity amplitudes with a 19-year global GNSS data set and reported enhanced winter daytime and summer nighttime variability. Regional studies give additional timing and process context: Cheng et al. (2021) reported a summer population near midnight over Taiwan, Le et al. (2024) described activity during LST 22-02 over Hong Kong, and Li et al. (2025) separated pre-midnight MSTID activity from later frequency spread F. These studies establish the broad seasonal pattern and show that warm-season nighttime variability contains more than one disturbance population.

The unresolved question for Hainan is not whether winter daytime and warm-season nighttime variability occur in East Asia, but what the local enhancements represent physically. A climatology alone cannot determine whether an enhancement develops with time over one region or appears as a satellite path crosses a horizontal structure. Hainan is well suited to this test because BeiDou GEO paths remain nearly fixed while IGSO and MEO paths move across the region, and earlier ionosonde and scintillation observations document organized nighttime spread F and scintillation in this sector (Wang et al., 2010; Shi et al., 2011).

We first establish daily-balanced VTEC and satellite-specific dTEC RMS climatologies from 1,793 represented dates between September 2015 and December 2020. We then use the contrast between nearly fixed and moving BeiDou sampling locations to determine how the winter and summer enhancements develop over Hainan. The central result is that winter structures evolve over or pass through the region and are seen consistently across the sampled directions, whereas the summer near-midnight increase is also time-dependent but is much more uneven across directions and regions.

https://doi.org/10.5194/egusphere-2026-5242
Preprint. Discussion started: 14 September 2026

2 Data and methods

The observations were collected at the site historically catalogued by the Chinese Meridian Project as Hainan Fuke Station (phase-I code FKT), now named Danzhou Station (phase-II station/product prefix ODAZH). The archive header gives 19.5 degrees N, 109.1 degrees E, and 89 m altitude; an independent RINEX position is 19.52676 degrees N, 109.1333 degrees E, and approximately 90 m. Its representative magnetic latitude is approximately 9.97 degrees N from the International Geomagnetic Reference Field for epoch 2020 (Alken et al., 2021), placing the site in the low-latitude Hainan sector.

The 2015-2020 measurements were recorded with a GPStation6 GNSS ionospheric scintillation and TEC receiver. The later GISMOR upgrade is outside the analyzed interval. The name 'GNSS Ionospheric TEC and Scintillation Monitor 02' in the current Chinese Meridian Project catalogue identifies the upgraded Danzhou product series rather than the historical receiver model. The Data Center reprocessed the GPStation6 observations with the updated algorithm used for the phase-II/GISMOR product, so the historical and current products share a processing definition although the hardware differs. Yusen Tian was the Data Center producer for the released historical product. The primary ATEC product-family record is DOI 10.12176/01.06.00588-V01 (NSSC, 2026a); the RINEX record DOI 10.12176/01.06.00578-V01 (NSSC, 2026b) was used only to check station position and viewing geometry. The study covers 23 September 2015 to 31 December 2020 and contains 1,793 represented UTC dates.

We assembled the 5 min observations into valid satellite arcs, daily VTEC cells, and satellite-specific dTEC RMS windows. Seasonal-local-time fields were calculated from daily medians and then examined for midnight timing, activity dependence, sampling support, filter response, and viewing geometry.

The source UTC date was the equal-weight unit in the climatologies and the resampling unit in the principal uncertainty estimates. Satellite-specific windows remained separate until the stated daily or hourly aggregation.

2.1 Building the VTEC and dTEC RMS climatologies

The background analysis used quality-controlled multi-satellite VTEC at 5 min cadence. Each accepted window contained at least three GPS or BeiDou satellites at elevations of 20 degrees or higher, giving 514,834 windows. Short-timescale variability was calculated from satellite-specific ATEC from the same constellations. Of 73,224,287 parsed records, 73,224,257 passed the basic azimuth, elevation, and non-negative-TEC checks. Local solar time (LST) was obtained from station longitude as LST = UTC + 26,184 s. Winter was December-February, spring March-May, summer June-August, and autumn September-November.

For the VTEC climatology, we first took the median of all accepted 5 min windows within each UTC-date, local-month, and one-hour LST cell, and then took the median across represented dates. This daily balancing prevents dates with more retained observations from dominating the climatology. Date bootstrap intervals describe the variability among observed days. We also repeated the monthly curves after restricting solar and geomagnetic activity and after giving available years equal weight, because autumn and the early part of the record sampled somewhat different activity and coverage conditions.

https://doi.org/10.5194/egusphere-2026-5242
Preprint. Discussion started: 14 September 2026

For dTEC, observations were separated into continuous satellite arcs when a gap exceeded 90 s or a UTC-date boundary was crossed. A 60 min centered running median represented the slowly varying background, with at least 75% of the nominal 30 s samples and two-sided temporal support. We defined dTEC(t) = ATEC(t) - median60min[ATEC(t)] and summarized its amplitude with a centered 30 min root-mean-square window, dTEC RMS = sqrt[(1/N) sum dTECi^2]. The 60/30 min combination retains variations on tens-of-minutes scales while removing most of the slower daily TEC change. Detrending choices can alter recovered disturbance periods and amplitudes (Osei-Poku et al., 2021; Guerra et al., 2024), so this operator is treated as a measurement definition and tested independently in Sect. 2.2.

The dTEC climatology used the same daily-balancing principle as VTEC: satellite-window medians were calculated within each date, month or season, and LST cell before dates were combined. The primary field contains 5,550,904 RMS windows in 41,119 daily month-LST cells. We matched VTEC and dTEC RMS cells to determine whether a larger background content was systematically associated with larger short-timescale variability. We also compared afternoon and nighttime sectors. Because midnight may lie on the next source date, the analysis was repeated using source UTC dates, local-calendar dates, and an observation-night definition that assigns LST 00-02 to the preceding evening. Hourly comparisons then located the summer change between LST 21 and 01.

These choices were checked for the specific biases they could introduce. We required progressively larger numbers of satellites per daily cell, repeated the climatologies with equal-year and common-year weighting and with one year omitted, and restricted the solar and geomagnetic activity range. Date-cluster and 3-7 day moving-block bootstrap intervals allowed for unequal sampling and persistence across consecutive days. Alternative hourly and satellite weighting schemes tested whether a few well-sampled paths determined the seasonal contrasts.

2.2 Using IPP motion to determine how the seasonal enhancements develop over Hainan

The climatologies establish when dTEC RMS is enhanced, but the physical meaning depends on whether the sampled signal changes at one ionospheric location or only changes as the satellite path crosses different locations. We therefore compared nearly fixed and moving IPPs as a targeted physical experiment. A nearly fixed IPP repeatedly samples approximately the same region, so an enhancement there requires local temporal evolution or a disturbance passing through that region. A moving IPP contains the same temporal contribution but can also cross horizontal bands, patches, gradients, or boundaries. Comparing the two groups therefore determines whether the seasonal enhancement is primarily shared in time or also changes substantially across the surrounding region.

IPP position and speed were calculated from azimuth and elevation at a 450 km thin shell. Fixed shell height affects mapped IPP position and therefore limits exact structure location (Xiang and Gao, 2019); the analysis uses broad motion classes rather than interpreting small position differences. Nearly fixed IPPs moved no faster than 0.2 km/min and moving IPPs moved at least 0.5 km/min; intermediate speeds were excluded. For each date and motion class, we subtracted the equal-width LST 13-14 median dTEC RMS from the LST 23-00 median. Negative values indicate larger afternoon variability and positive values indicate larger near-midnight variability.

https://doi.org/10.5194/egusphere-2026-5242
Preprint. Discussion started: 14 September 2026

Motion class is closely related to BeiDou orbit geometry: the nearly fixed observations are supplied almost entirely by GEO satellites, whereas IGSO and MEO satellites supply nearly all moving observations. We therefore treated orbit type and satellite composition as part of the mechanism test rather than as independent confirmation. We summarized the night-minus-afternoon contrast for individual satellites and for the GEO, IGSO, and MEO groups, and repeated the complete comparison after removing each of the 16 observed satellites in turn. These tests determine whether a seasonal sign is distributed across several viewing paths or is carried by one satellite.

The two motion classes can also view different directions. We first balanced them within common 10 degree elevation bands and then repeated the calculation within common 10 degree elevation by 45 degree azimuth sectors. The elevation-only comparison retained broad directional coverage and included 442 paired summer dates and 385 paired winter dates. Joint elevation-azimuth matching reduced the common support to 114 summer dates and 174 winter dates. Date bootstrap intervals used 10,000 resamples. The strict comparison is therefore a directional diagnostic, while the elevation-matched comparison remains the better-supported estimate of the regional contrast. Alternative speed thresholds, minimum satellite support, activity restrictions, moving-block resampling, leave-one-year-out estimates, and speed bins tested whether the result followed sample composition, viewing direction, or IPP speed itself.

The same framework was applied month by month in spring and autumn. March, April, and May were examined separately to follow the loss of the winter-afternoon pattern and the development of the warm-season near-midnight pattern. September, October, and November were examined in the reverse order. This monthly analysis avoids treating each transition season as one uniform physical state.

Finally, we tested whether the 60/30 min operator could create or suppress the apparent differences. Background windows of 60 and 120 min were combined with RMS windows of 10, 30, and 60 min. Because all of these choices use the same nonlinear running-median/RMS method, we also passed smooth cubic-polynomial and 180 min-knot spline arcs through the reference chain to measure leakage in the absence of imposed short-period variability. Sinusoids with periods of 20-120 min, amplitudes of 0.02-0.10 TECU, and four phases were then injected into smooth arcs to measure how much amplitude the operator retained. These tests bound the part of the observed climatology that could arise from background curvature or filter attenuation before the IPP differences are interpreted physically.

3 Results

Figure 1 summarizes the sampling context for the climatologies. Panels 1a-1c show that the record is nearly complete during 2016-2018, less complete in parts of 2015 and 2019, and concentrated in the declining phase of solar cycle 24. Panel 1b shows that annual reweighting changes local amplitudes more than the broad month-LST fields. Panel 1d introduces the matched VTEC-dTEC comparison discussed in Sect. 3.3.

https://doi.org/10.5194/egusphere-2026-5242
Preprint. Discussion started: 14 September 2026

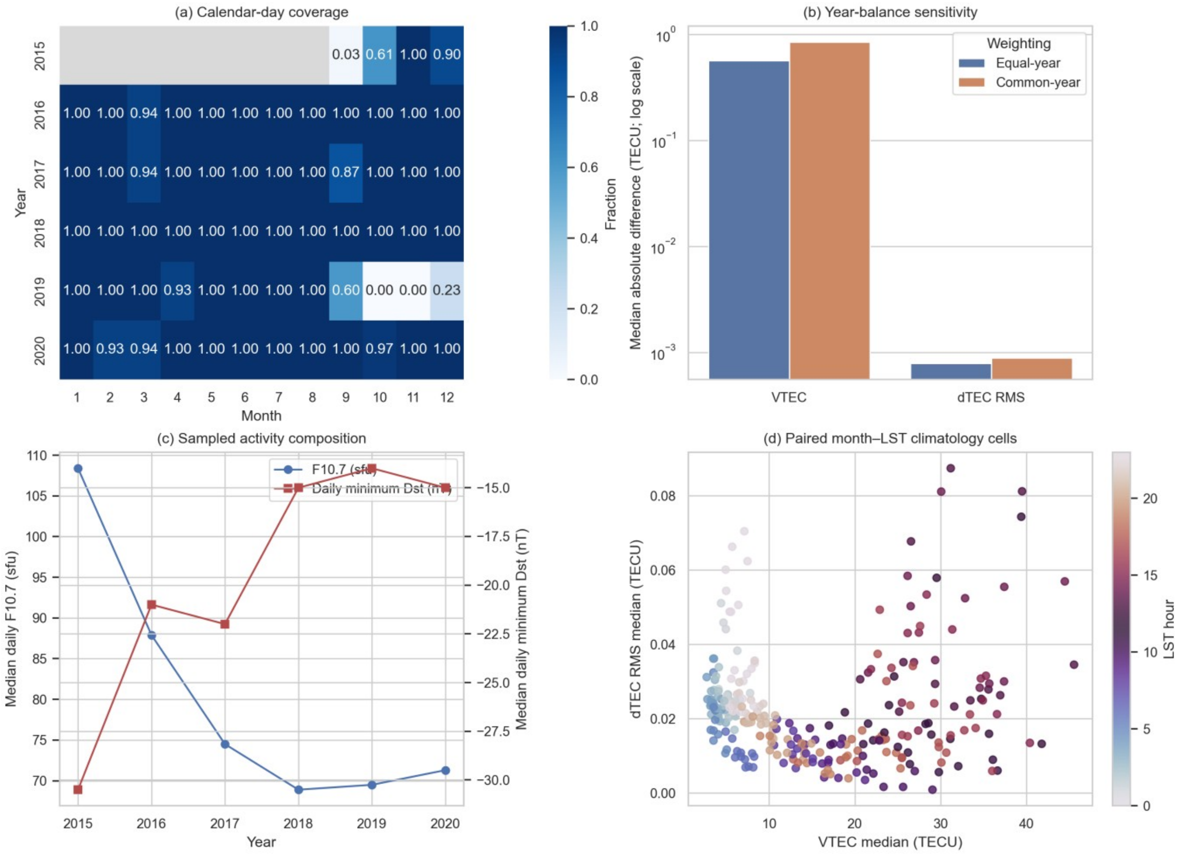

Figure 1. Coverage, annual composition, and the VTEC-dTEC comparison. (a) Fraction of calendar days represented by source year and month; grey cells precede the study period. (b) Median absolute difference between the pooled climatology and equal-year or common-year alternatives. (c) Annual medians of daily F10.7 and daily minimum Dst on represented dates. (d) The 276 paired month-LST climatology cells, coloured by LST. Full numerical values and Kp summaries are provided in the machine-readable companion tables.

3.1 Seasonal and local-time changes in the Hainan VTEC background

Figure 2a shows the same basic daily VTEC cycle in every month: a minimum before dawn, rapid growth after sunrise, a post-noon maximum, and a nighttime decline. The lowest values occur mainly at LST 04-05 and the monthly maxima at LST 13-16. Against this stable daily shape, the daytime amplitude and peak time change substantially through the year.

The strongest background occurs in October, while March-April and November also have high daytime VTEC (Figure 2a). July has the smallest daytime maximum, and the July-August maximum is delayed to about LST 16, two to three hours later than in most winter, spring, and late-autumn months. Figure 2b shows that day-to-day uncertainty is smallest at night and broadest near the daytime maxima, but the October enhancement and midsummer delay remain clear in the month-LST field.

https://doi.org/10.5194/egusphere-2026-5242
Preprint. Discussion started: 14 September 2026

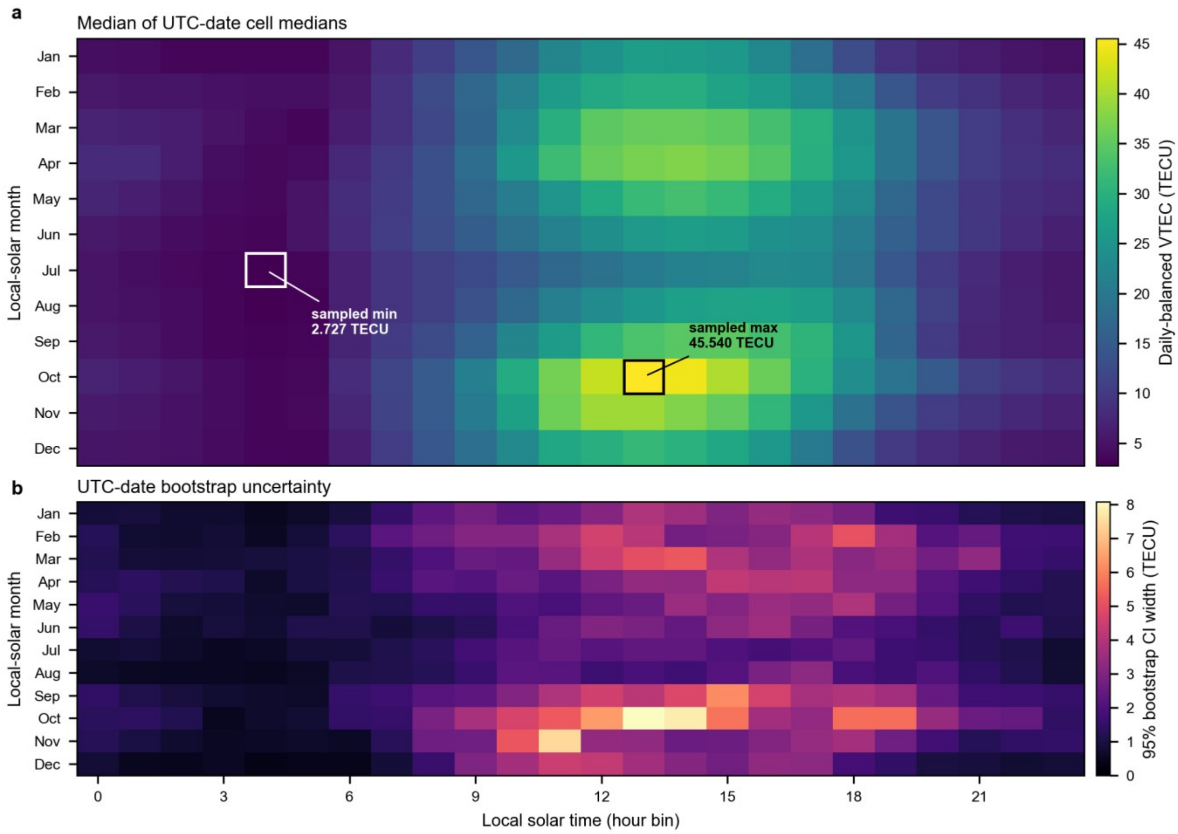

Figure 2. Daily-balanced VTEC month-LST climatology. (a) Median of UTC-date cell medians. (b) Width of the 95% UTC-date bootstrap interval based on 1000 replicates. Boxes identify the sampled global minimum and maximum only as quantitative anchors; interpretation is based on the broader month-LST structure.

Figure 3a asks whether the autumn maximum is only a consequence of the solar and geomagnetic conditions sampled in different months. After restricting the analysis to daily maximum Kp no greater than 3, daily minimum Dst no lower than -30 nT, and daily median F10.7 between 65 and 90 sfu, October remains the strongest monthly maximum, with November and April next. The autumn ordering therefore persists within a substantially narrower activity range.

https://doi.org/10.5194/egusphere-2026-5242
Preprint. Discussion started: 14 September 2026

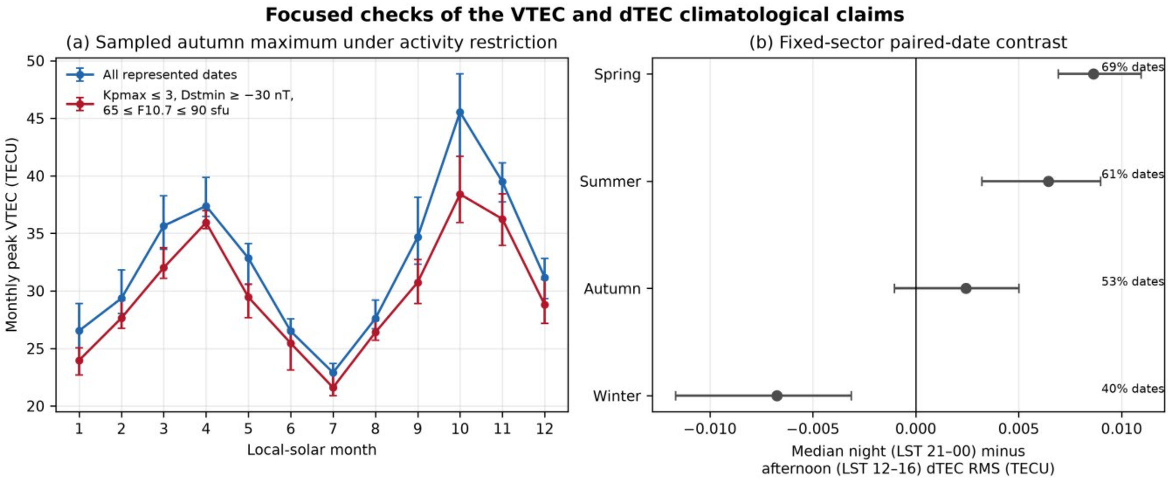

Figure 3. Focused tests of the principal climatological contrasts. (a) Monthly peak VTEC for all represented dates and after the joint restriction of daily maximum Kp ≤ 3, daily minimum Dst ≥ -30 nT, and daily median F10.7 between 65 and 90 sfu. Error bars are 95% UTC-date bootstrap intervals with the peak LST reselected in every replicate. (b) Seasonal paired-date differences between late evening/midnight (LST 21-00) and afternoon (LST 12-16). Positive values favor nighttime variability and negative values favor afternoon variability; error bars are 95% paired-date bootstrap intervals, and labels give the fraction of dates with larger nighttime dTEC RMS.

3.2 Seasonal and local-time changes in dTEC RMS

Figure 4 shows that the dTEC RMS field does not follow the VTEC background cycle. Two broad enhancements are visible: an afternoon feature that is strongest in the cold season and a late-evening to midnight feature that grows during spring and summer. Winter peaks near LST 13, whereas spring and summer peak near LST 23-00. The autumn field contains both components and is less clearly dominated by one local-time sector.

The seasonal change is gradual rather than a switch between four uniform three-month states (Figure 4a). The preferred local time moves from the afternoon in winter toward the nighttime sector through spring, remains near midnight in summer, and returns toward the afternoon during autumn. The hours of minimum variability also move with season, confirming that one fixed local-time curve cannot describe the annual dTEC pattern.

https://doi.org/10.5194/egusphere-2026-5242
Preprint. Discussion started: 14 September 2026

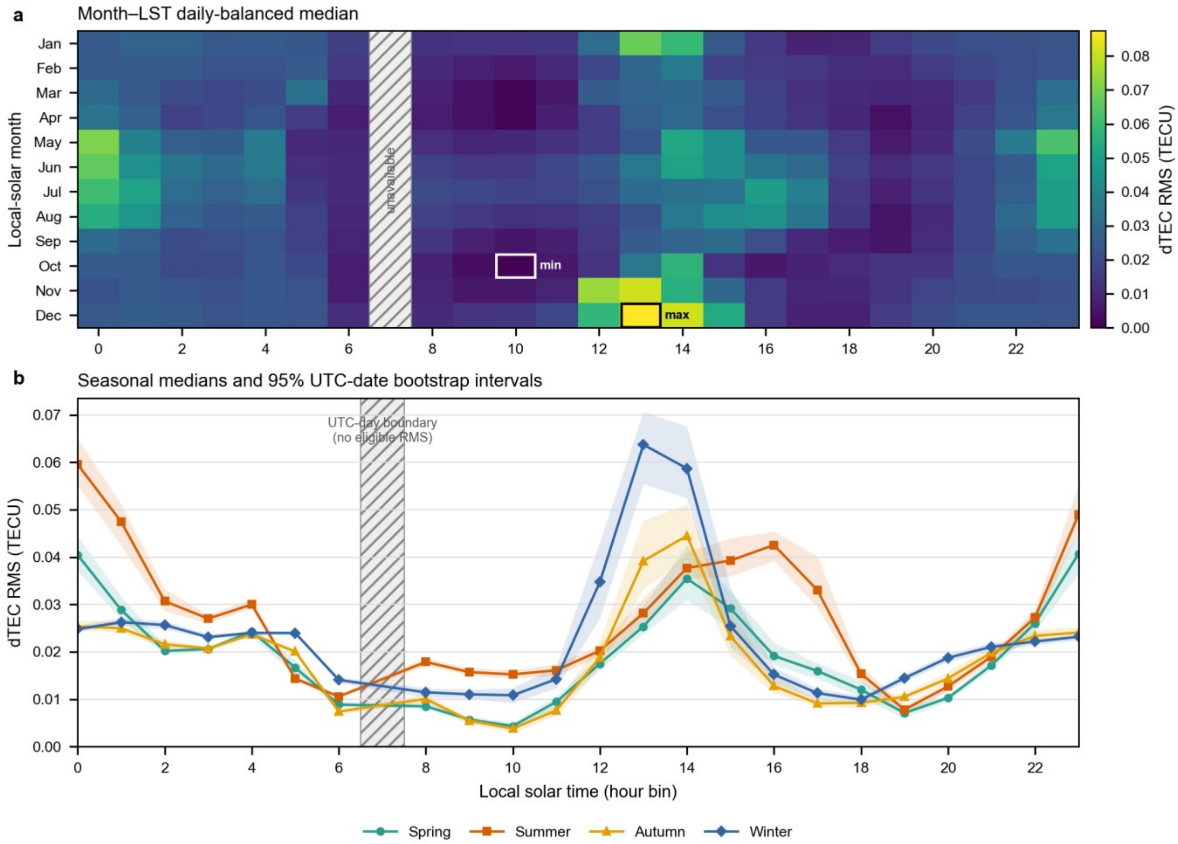

Figure 4. Daily-balanced dTEC RMS climatology for the primary 60 min background and 30 min RMS windows. (a) Month-LST medians. (b) Seasonal medians with 95% UTC-date bootstrap intervals. LST 07 is hatched because centered processing lacks two-sided support across the daily-product boundary.

3.3 From individual satellite traces to the winter-afternoon and warm-season midnight patterns

Figure 5 gives trace-level examples of the two patterns before they are summarized statistically. The six illustrative dates were chosen from well-covered winter afternoons and summer near-midnight intervals with at least three continuously observed satellites, without selecting individual traces by dTEC amplitude. The displayed winter date shows many satellite paths increasing together in the afternoon, whereas the summer date concentrates the increase around LST 23-00. The cases connect the climatological patterns with their appearance in individual observations.

https://doi.org/10.5194/egusphere-2026-5242
Preprint. Discussion started: 14 September 2026

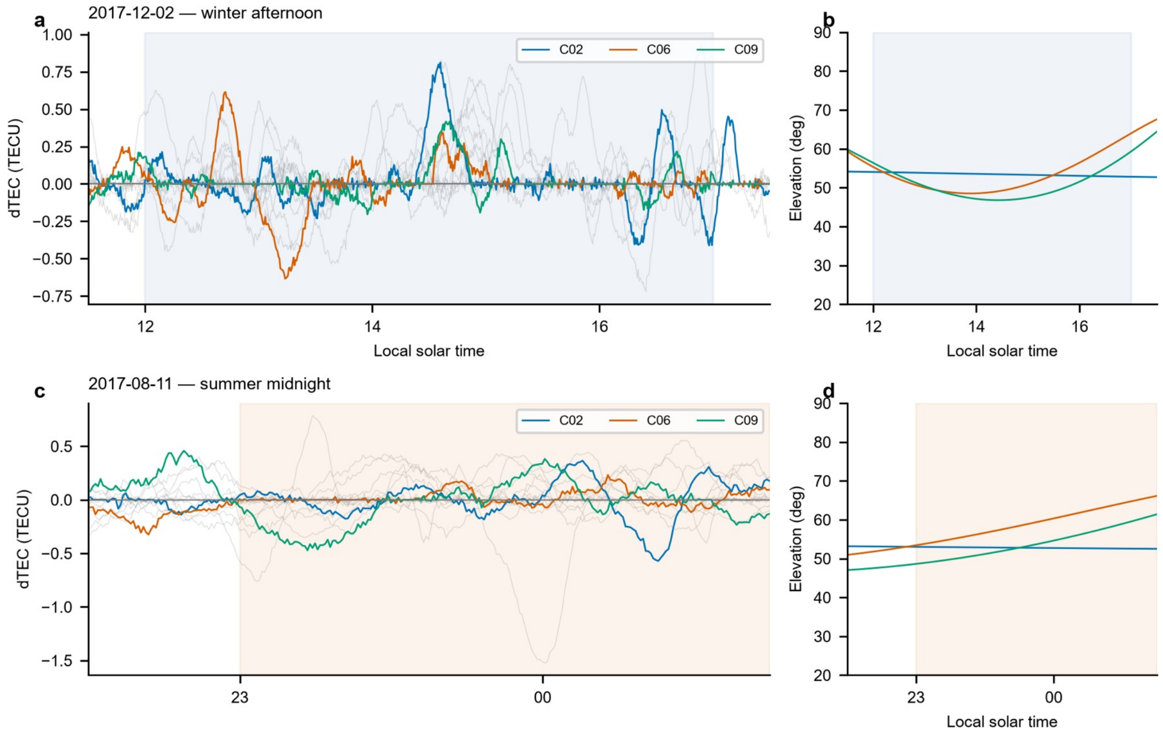

Figure 5. Illustrative multi-satellite examples of the winter-afternoon and summer near-midnight patterns. Thin gray curves show all eligible dTEC traces. Colored traces were highlighted by coverage and elevation proximity to 55 degrees. Target and control sectors are shaded, and lower panels show satellite elevation.

The matched VTEC-dTEC comparison in Figure 1d shows that short-timescale variability is not simply larger whenever the background plasma content is larger. Across daily cells the rank association is weak (-0.159), and it becomes still weaker after the typical month-LST pattern is removed. The VTEC quartiles are also non-monotonic: enhanced dTEC RMS occurs in both low-VTEC nighttime cells and high-VTEC afternoon cells. The two climatologies therefore describe related but different parts of the ionosphere.

Figure 3b quantifies the seasonal change seen in Figure 4 by comparing late evening and midnight (LST 21-00) with afternoon (LST 12-16) on paired dates. Winter is consistently afternoon-dominant, spring and summer are nighttime-dominant, and autumn lies near the transition between them. The same signs remain when activity, annual weighting, satellite support, and consecutive-day dependence are restricted.

Figure 6 locates the summer feature more precisely. When midnight is excluded, the summer contrast between LST 21-23 and 12-16 is indistinguishable from zero. With observation nights defined so that LST 00-02 belongs to the preceding evening, the summer difference begins to turn positive after LST 22, is largest near LST 00, and remains positive at LST 01. Spring shows a related late-evening rise. Thus the warm-season enhancement is centered near midnight rather than representing the whole evening sector.

https://doi.org/10.5194/egusphere-2026-5242
Preprint. Discussion started: 14 September 2026

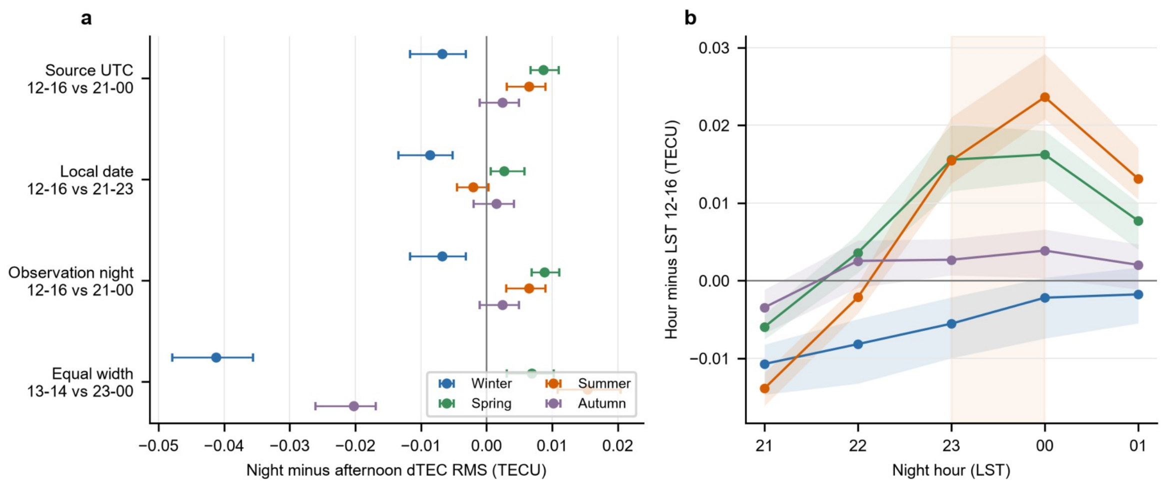

Figure 6. Date assignment and timing of the seasonal dTEC RMS contrasts. (a) Source-UTC, local-calendar, and observation-night sector definitions. (b) Hourly observation-night differences relative to LST 12-16 with 95% date-cluster bootstrap intervals. The local-calendar summer comparison excludes midnight and has an interval spanning zero, while LST 23-01 contains the positive summer increase.

3.4 Winter structures evolve over Hainan, while summer structures are horizontally uneven

Figure 7 shows that the winter-afternoon enhancement is present whether the sampled ionospheric location remains nearly fixed or moves across the region. Both groups stay afternoon-dominant before and after elevation matching. The winter maximum therefore requires the TEC structure to change with time over Hainan or to pass through the sampled region. A stationary horizontal gradient revealed only by a moving satellite path cannot produce the shared winter pattern.

Figure 7 also shows that the summer near-midnight enhancement contains a real temporal increase. After elevation matching, it remains positive where the IPP is nearly fixed as well as where the IPP moves across the region. The increase therefore occurs at repeatedly sampled locations and is not created only when a moving path crosses a pre-existing gradient. The larger response along moving paths in the broader sample indicates that some of the directions and regions crossed by those paths contain stronger structures.

Figure 8 connects the winter and summer end members month by month. In March, nearly fixed IPPs retain an afternoon-dominant pattern while moving paths lie near zero. April is a crossover month, and by May both groups are night-dominant after elevation matching. The reverse development occurs in autumn: September retains a weak nighttime component, October lies near the crossover, and November is clearly afternoon-dominant. The confidence intervals and paired-date support for each month are reported in Table S17.

Figure 9a shows that motion class and orbit family are closely coupled. Nearly fixed windows are almost entirely GEO observations, whereas moving windows are dominated by IGSO observations with limited MEO support. The comparison therefore tests the combined observational properties of motion, orbit, direction, and sampled region; it is not an estimate of a causal response to IPP speed.

https://doi.org/10.5194/egusphere-2026-5242
Preprint. Discussion started: 14 September 2026

Figure 9b shows that the winter and summer structures differ in their horizontal distribution. GEO and IGSO groups both retain the winter-afternoon and summer near-midnight signs in their aggregate statistics. Winter signs are consistent across adequately sampled GEO satellites. Summer estimates vary much more among satellites: some directions show a clear near-midnight increase, while others lie near zero or have the opposite sign. The summer enhancement is therefore concentrated more strongly in some sampled regions or directions than in others.

Deleting any one satellite preserves the winter-afternoon pattern and the positive summer contrasts when elevation is matched (Figure 9c), showing that neither seasonal pattern is carried by one satellite. The stricter direction comparison in Figure 9d clarifies the physical difference. Winter remains afternoon-dominant in both motion classes and the two estimates agree within uncertainty. In summer, the moving-path increase weakens to approximately zero within common elevation-azimuth sectors, while the near-fixed increase remains positive. Thus the summer moving-path advantage in the broader sample comes from the directions and regions those paths cover, not from motion speed. Taken together, Figures 7-9 show a winter disturbance pattern that evolves in time across the sampled sector and a summer near-midnight increase that also evolves in time but is much less evenly distributed horizontally.

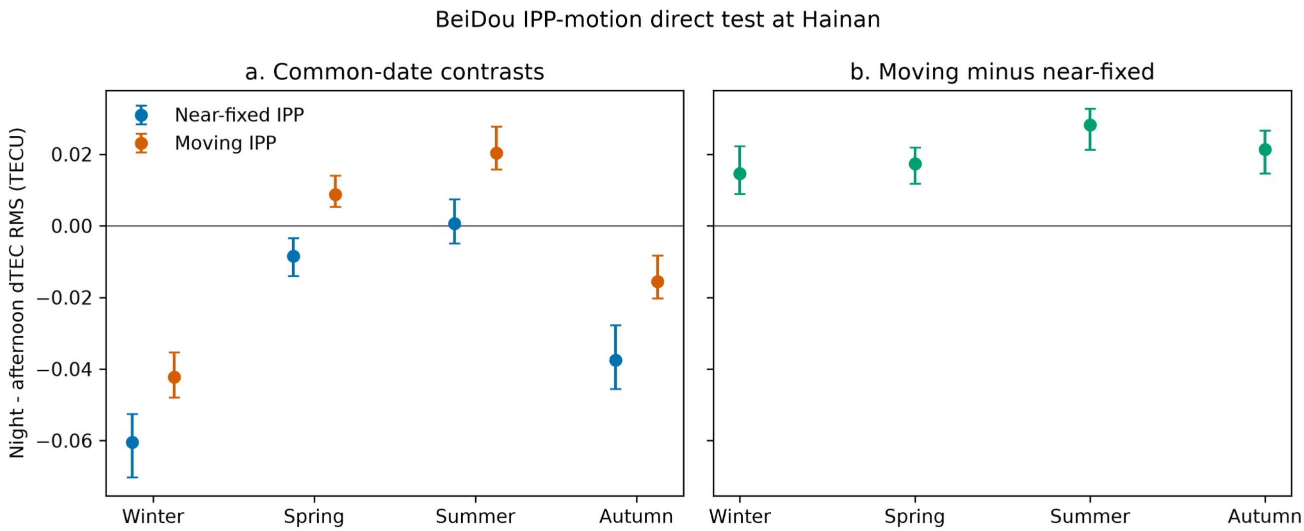

Figure 7. Common-date BeiDou comparison of nearly fixed and moving IPPs. (a) Seasonal LST 23-00 minus LST 13-14 dTEC RMS contrasts; negative values favor afternoon variability and positive values favor near-midnight variability. (b) Paired moving-minus-nearly-fixed differences. Error bars are 95% paired-date bootstrap intervals. Elevation-matched and joint elevation-azimuth-matched estimates, intervals, and paired-date counts are summarized in Table 1 and Table S16.

https://doi.org/10.5194/egusphere-2026-5242
Preprint. Discussion started: 14 September 2026

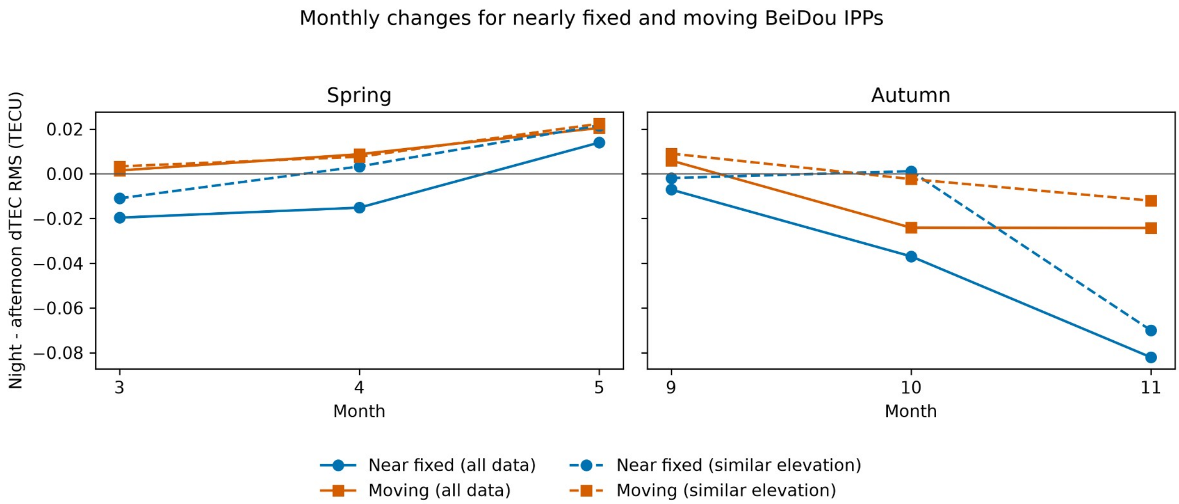

Figure 8. Month-by-month transition of the night-minus-afternoon dTEC RMS contrast for nearly fixed and moving BeiDou IPPs. Negative values indicate larger afternoon variability and positive values indicate larger near-midnight variability. Solid lines use all common-date observations; dashed lines balance the two motion classes within common elevation bands. Spring progresses from an afternoon pattern in March to a near-midnight pattern in May, while autumn develops in the opposite direction from September to November. Bootstrap intervals and paired-date support are given in Table S17.

https://doi.org/10.5194/egusphere-2026-5242
Preprint. Discussion started: 14 September 2026

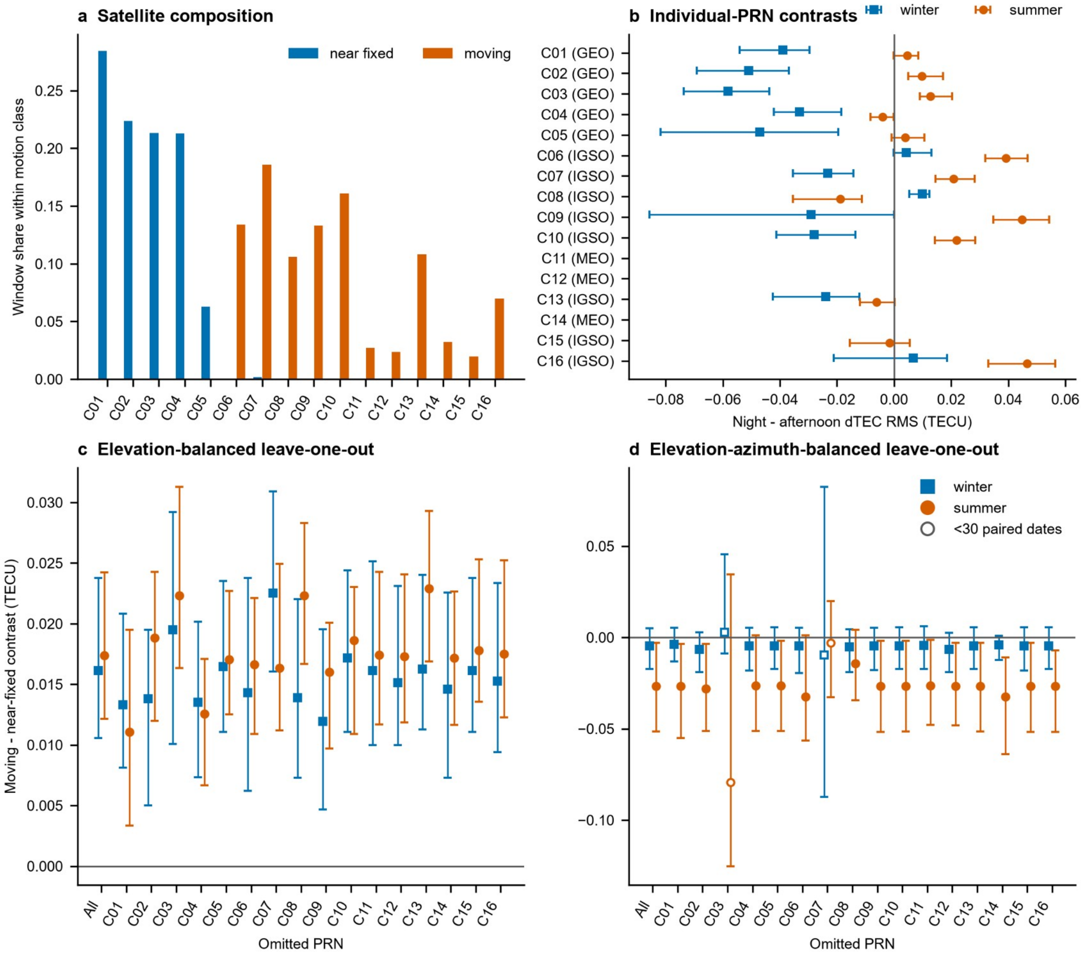

275 **Figure 9. Satellite composition and robustness of the IPP comparison. (a) Satellite contributions to nearly fixed and moving classes. (b) Individual-satellite winter and summer contrasts with 95% date-bootstrap intervals; estimates with fewer than 30 paired dates are omitted. (c) Moving-minus-nearly-fixed differences after omitting each satellite and balancing elevation. (d) The same analysis with joint elevation and azimuth balancing. Open symbols mark fewer than 30 paired dates. Orbit, PRN, leave-one-out, and sample-support values are reported in Tables S18-S30.**

https://doi.org/10.5194/egusphere-2026-5242
Preprint. Discussion started: 14 September 2026

Table 1. Primary same-date IPP contrasts. Values are median dTEC RMS contrasts in TECU with 95% date-bootstrap intervals. Moving - fixed is the median of the date-wise paired differences and therefore need not equal the difference between the two marginal medians; n is the number of paired dates.

Season	Geometry	n	Moving	Nearly fixed	Moving - fixed
Winter	Elevation	385	-0.02583 [-0.03564, -0.01657]	-0.05219 [-0.06852, -0.03991]	0.01614 [0.01056, 0.02378]
Summer	Elevation	442	0.02128 [0.01711, 0.02600]	0.00823 [0.00464, 0.01222]	0.01738 [0.01214, 0.02424]
Winter	Elevation + azimuth	174	-0.06030 [-0.09021, -0.02526]	-0.05353 [-0.07321, -0.04060]	-0.00458 [-0.01745, 0.00489]
Summer	Elevation + azimuth	114	0.00169 [-0.01843, 0.01732]	0.01691 [0.00505, 0.03271]	-0.02666 [-0.05152, -0.00300]

4 Discussion

4.1 Physical meaning of the Hainan VTEC and dTEC RMS climatologies

VTEC represents the plasma maintained by solar production, chemical loss, neutral winds, and equatorial electrodynamic transport. The pre-dawn minimum and post-noon maximum in Figure 2 are therefore the expected background response of the low-latitude ionosphere. The autumn daytime enhancement remains after activity restriction (Figure 3a), pointing to a seasonal contribution from the coupled thermosphere-ionosphere system. The delayed July-August maximum indicates that midsummer changes not only the amount of daytime plasma but also the time at which it accumulates.

This background agrees with the post-noon maximum and equinoctial enhancement reported over southern China by Wu et al. (2012). The six-year Hainan record adds a local detail: October is stronger than the sampled spring months, and the midsummer maximum occurs later in the afternoon. These are modest regional differences, but they define the background in which shorter disturbances develop.

The dTEC RMS climatology describes a different physical property. Its weak and non-monotonic relation with VTEC means that a large plasma content is neither necessary nor sufficient for large short-timescale changes. VTEC mainly follows the production, loss, and transport of the background plasma, whereas dTEC RMS is more sensitive to waves, instability growth, drifting gradients, and irregularity boundaries. Their displaced maxima therefore show that the strongest background plasma and the strongest short-timescale structuring are controlled by different combinations of processes.

Earlier East Asian event, occurrence, and amplitude studies established the broad winter-daytime and warm-season-nighttime pattern (Ding et al., 2011; Hu et al., 2021; Cheng et al., 2021; Le et al., 2024; Li et al., 2024; Zhang et al., 2026). The Hainan analysis adds two linked results. First, VTEC and dTEC RMS are placed in the same date-balanced climatological framework, showing that background plasma content and short-timescale structuring peak in different seasons and local-time sectors. Second, the IPP comparison tests the observational character of the dTEC RMS enhancements and shows that winter and summer do not respond to viewing geometry in the same way.

https://doi.org/10.5194/egusphere-2026-5242
Preprint. Discussion started: 14 September 2026

The Hainan summer rise after LST 22 and maximum near midnight agree with the near-midnight summer population over Taiwan, the LST 22-02 interval reported over Hong Kong, and the sequence of pre-midnight MSTIDs followed by later frequency spread F over China (Cheng et al., 2021; Le et al., 2024; Li et al., 2025). Those studies primarily identify events, occurrence rates, or propagation classes. The Hainan record instead follows the amplitude of all eligible observations, including weaker or unclassified structure, and shows how the daytime-to-nighttime preference develops from March to May and reverses from September to November. The IPP comparison then tests whether each enhancement develops in time and how evenly it is distributed around the station.

4.2 Winter temporal evolution and the uneven horizontal distribution of summer structures

The IPP comparison gives the seasonal climatology a physical interpretation. A nearly fixed BeiDou path repeatedly samples approximately the same ionospheric region, whereas a moving path crosses successive locations. Enhancement shared by both classes must develop with time at a location or pass through that location. Differences among paths then reveal how unevenly the enhanced structures are distributed, after orbit family and viewing direction are considered.

The winter-afternoon enhancement reflects short-timescale TEC structures that evolve over Hainan or pass through the region. The enhancement appears at nearly fixed and moving IPPs, in GEO and IGSO groups, after every single-satellite deletion, and after elevation and azimuth are jointly matched. Under the strict comparison the two motion classes agree within uncertainty (Table 1). This combination cannot be explained by a stationary horizontal gradient sampled only by a moving ray. The winter maximum therefore contains a real temporal disturbance component, either through local growth and decay or through a wave-like structure passing the nearly fixed sampling region.

This behavior is consistent with the winter daytime MSTID and gravity-wave environment reported over China (Ding et al., 2011; Hu et al., 2021). Daytime gravity-wave forcing, electrodynamic coupling, and the background winter ionosphere can produce traveling or evolving TEC structures that pass both fixed and moving lines of sight. The present data do not distinguish local growth from horizontal propagation, but they show that the winter climatological maximum is a temporal disturbance pattern over Hainan rather than an apparent change generated only by satellite motion.

Summer also contains a real time-dependent near-midnight enhancement. It appears in the full climatology, in aggregate GEO and IGSO observations, and at nearly fixed IPPs after elevation matching. The increase can therefore develop at a repeatedly sampled location and does not require a moving ray to reveal it.

Unlike the winter pattern, the summer enhancement is not distributed evenly around Hainan. Individual satellites do not show the same response, and the apparent moving-path advantage reverses when elevation and azimuth are jointly matched. The most direct interpretation is that the near-midnight environment favors enhanced short-timescale structure, but the stronger structures occupy only part of the surrounding region or extend preferentially along particular directions. Moving IPPs cross more of the region and may encounter strong bands, patches, gradients, or irregularity boundaries. Their larger elevation-matched amplitude reflects what they sample, not an effect caused by IPP speed.

https://doi.org/10.5194/egusphere-2026-5242
Preprint. Discussion started: 14 September 2026

The evidence identifies a genuine near-midnight temporal increase within a horizontally uneven ionosphere. A single receiver cannot reconstruct the structures quantitatively because each measurement is a line-of-sight TEC integral and the ionosphere evolves while the IPP moves. The present experiment identifies temporal enhancement together with directional and regional variation, but a receiver array is needed to determine wavelength, horizontal extent, orientation, propagation speed, and the separate temporal and spatial contributions to amplitude.

A plausible warm-season environment includes nighttime MSTIDs together with gradients or boundaries associated with spread F and plasma-bubble evolution. Central and southern China observations show horizontally banded nighttime MSTIDs whose TEC signatures depend on satellite motion, while Hainan observations report near-midnight MSTIDs, spread F, scintillation, and plasma-bubble-related structure (Huang et al., 2018; Wang et al., 2010; Shi et al., 2011; Sun et al., 2016). The Hainan amplitude climatology does not assign every window to one category. It instead shows that the summer population is compatible with evolving disturbances that have appreciable and direction-dependent horizontal organization.

Spring and autumn show how the dominant disturbance environment changes between these winter and summer states. March retains a winter-like afternoon response at nearly fixed locations. April lies near the crossover, and by May both motion classes are night-dominant after elevation matching. September retains a weak warm-season nighttime component, October lies near the transition, and November returns to an afternoon-dominant pattern. The transition is therefore an ordered replacement of a broadly sampled winter temporal pattern by a near-midnight pattern that is more uneven across the region, and the reverse replacement occurs in autumn.

Several coupled processes may contribute to this replacement. Background density and EIA configuration change the plasma in which disturbances develop. Seasonal neutral winds and gravity-wave propagation affect daytime wave signatures, while E-region conductivity, sunset electrodynamics, and nighttime instability growth affect MSTIDs, spread F, and plasma-bubble boundaries after dusk. The observations do not select one driver, but they show when the dominant physical environment changes: the winter-like temporal pattern remains visible in March, the uneven near-midnight pattern is evident by May, and the return to the winter state is largely complete by November.

4.3 Robustness of the climatological and IPP interpretations

The sampling checks address whether the seasonal fields are products of uneven coverage rather than ionospheric behavior. Requiring at least 3, 5, or 8 satellites retains 99.87%, 99.26%, and 96.78% of daily cells, and the eight-satellite field remains almost identical to the one-satellite baseline. Equal-year, common-year, leave-one-year-out, activity-restricted, and 3-7 day block-bootstrap analyses retain the autumn VTEC enhancement and the winter-afternoon to warm-season-nighttime dTEC ordering. These tests support the broad seasonal interpretation even though individual amplitudes and peak hours vary.

Figure 10 shows that changing the running-median and RMS windows alters the absolute dTEC RMS amplitude, but the main seasonal timing remains visible. Smooth inputs produce localized residuals near curvature extrema, with arc-level leakage overlapping the size of small summer contrasts. The smooth-null summer sector difference is centered near zero for moving IPPs. For near-fixed IPPs, the spline baseline is centered at zero and the polynomial baseline is negative; neither

https://doi.org/10.5194/egusphere-2026-5242
Preprint. Discussion started: 14 September 2026

produces the observed systematic positive direction in the validation sample. This supports interpreting the positive near-fixed summer contrast as a temporal enhancement rather than the natural sign of smooth-background leakage. The winter sign also persists across motion classes, satellites, and direction matching. The robust evidence is therefore the seasonal timing and cross-geometry consistency; absolute dTEC RMS amplitudes remain specific to the stated 60/30 min operator.

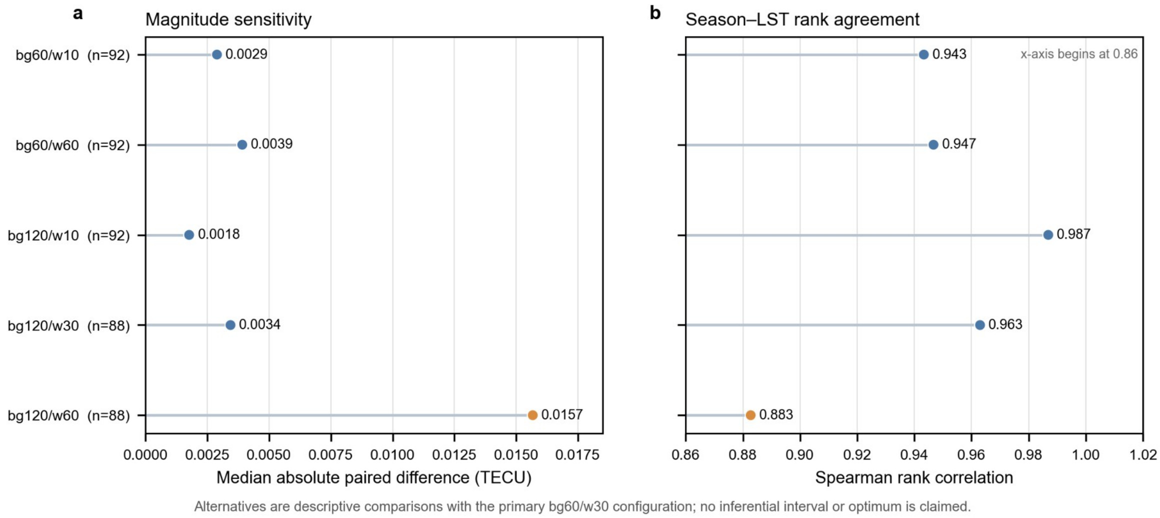

Figure 10. Sensitivity of dTEC RMS to background and RMS-window duration. Each alternative is paired with the primary 60 min background/30 min RMS field. Smooth-signal leakage and sinusoidal response of the reference processing method are shown in Fig. S8 in the Supplement.

Figure 11 shows that reasonable changes in minimum elevation and arc-gap threshold do not reorganize the record-level field. Together with the elevation-matched IPP result, this reduces the likelihood that the winter and summer contrasts are produced by one arbitrary quality-control choice. The stricter joint elevation-azimuth comparison has fewer dates, however, so the directional interpretation should be tested with a regional receiver array rather than treated as a complete map of the structure.

https://doi.org/10.5194/egusphere-2026-5242
Preprint. Discussion started: 14 September 2026

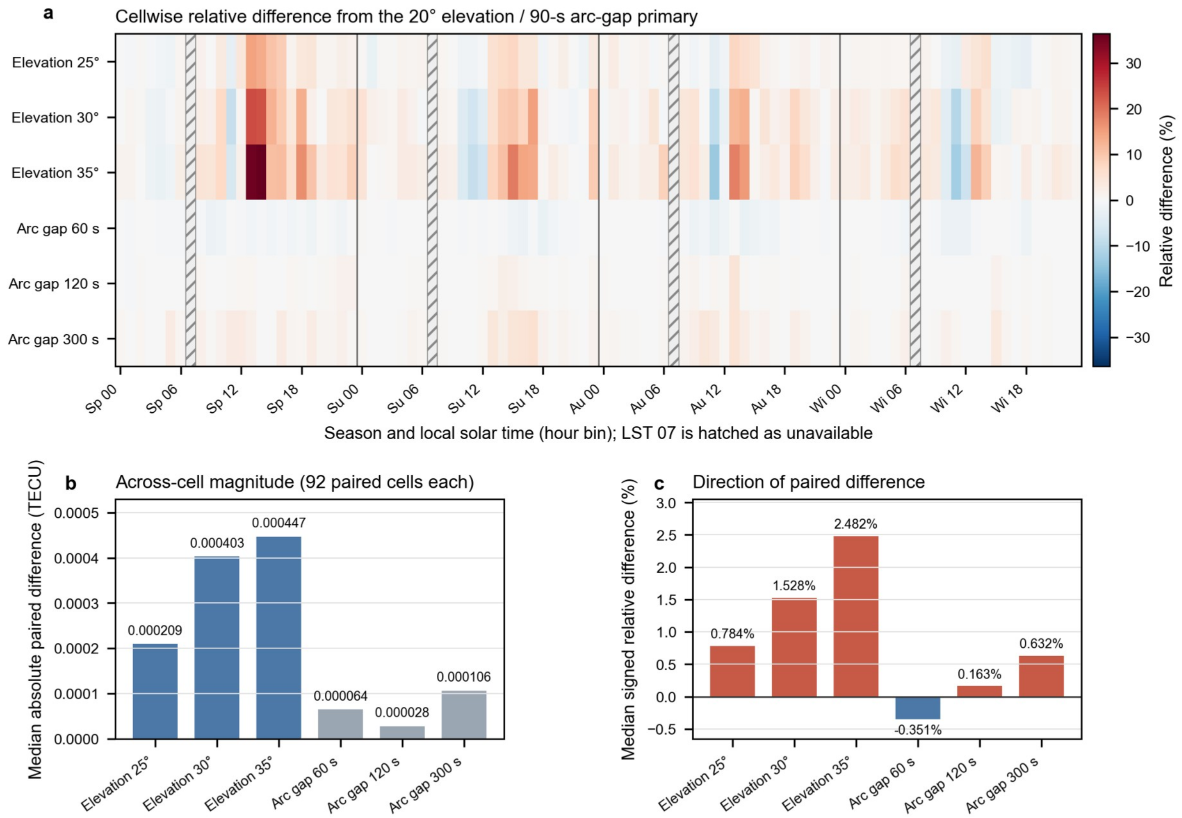

Figure 11. Record-level sensitivity to minimum elevation and arc-gap threshold. (a) Cellwise relative differences from the 20°/90 s reference. (b) Median absolute paired differences. (c) Median signed relative differences. All alternatives were recomputed before arc construction and background estimation.

Nearby receivers can test whether the LST 23-01 structures appear at the same time across the region, whether their amplitudes depend systematically on direction, and whether a disturbance boundary moves from one line of sight to another. Combining fixed BeiDou paths, moving GNSS paths, ionosonde height and spread-F measurements, scintillation, airglow, and neutral winds would help distinguish nighttime MSTIDs from plasma-bubble or spread-F boundaries and other gradients. The present analysis predicts that the near-midnight enhancement should remain detectable at fixed locations but vary among viewing directions, whereas the winter-afternoon enhancement should remain visible even where the viewing point moves little. These are directly testable regional signatures of the temporal and horizontal components identified here.

5 Conclusions

Six years of Hainan observations show that background VTEC and short-timescale dTEC RMS describe different parts of the low-latitude ionosphere. VTEC follows daytime plasma buildup, is strongest in autumn, and peaks later in midsummer.

https://doi.org/10.5194/egusphere-2026-5242
Preprint. Discussion started: 14 September 2026

dTEC RMS instead changes from a winter-afternoon maximum to a warm-season near-midnight maximum, with an ordered transition from March to May and the reverse development from September to November.

The winter-afternoon enhancement reflects short-timescale TEC structures that evolve over or pass through Hainan. Its presence across nearly fixed and moving sampling locations and comparable viewing directions rules out a stationary horizontal gradient as the sole explanation. The summer near-midnight enhancement also develops with time, because it remains visible at repeatedly sampled locations. Its strength, however, changes markedly across directions and sampled regions. The summer structures are therefore more likely concentrated in particular parts of the Hainan sector or extended along preferred directions than spread uniformly. Regional observations are needed to determine their shapes, scales, and propagation.

Code availability

The Python workflow used to calculate the climatologies, IPP comparisons, validation tests, and manuscript figures is prepared as version 1.1.0 under the MIT License. Two reviewer-access archives accompany the submission: the version 1.0.0 core workflow and the version 1.1.0 validation extension. They contain the code, configuration, tests, expected-result snapshots, and reproduction instructions. A public software archive has not yet been registered.

Data availability

The historical 2015-2020 GPStation6 observations were reprocessed and released by the Chinese Meridian Project Data Center using the updated product algorithm. The current Danzhou level-2 vertical absolute TEC product-family record is available from the National Space Science Data Center (NSSC, 2026a; https://doi.org/10.12176/01.06.00588-V01); this catalogue record documents the current product series and is not presented as the container of the historical files analysed here. Official source files remain with the provider. The Danzhou RINEX product-family record was used only for the station-position and viewing-geometry checks (NSSC, 2026b; https://doi.org/10.12176/01.06.00578-V01). Solar and geomagnetic indices were obtained from the NASA Space Physics Data Facility OMNI Hourly Data Set (Papitashvili and King, 2020; https://doi.org/10.48322/1shr-ht18; accessed 15 August 2026).

Author-generated figure source data and derived statistics are publicly available from Science Data Bank in the record 'Figure source data and derived statistics for seasonal reorganization and near-midnight localization of short-timescale TEC variability over low-latitude Hainan' (version 1.0.0, CC BY 4.0; Wang and Tian, 2026; https://doi.org/10.57760/sciencedb.00zln). The repository contains the processed data deposited for this study and excludes Chinese Meridian Project and NASA source files. The additional summary tables supporting the current IPP analysis are included in the Supplement submitted with this manuscript.

https://doi.org/10.5194/egusphere-2026-5242
Preprint. Discussion started: 14 September 2026

Author contributions

ZW: Conceptualization, Methodology, Writing - original draft, Writing - review and editing, Supervision, and Project administration. YT: Analysis, Visualization, and Data curation. GC: Methodology, Validation, and Writing - review and editing. GW: Analysis and Validation. GT: Data curation and Visualization. KD: Validation. YZ: Writing - review and editing. XW: Data curation. All authors approved the submitted version.

Competing interests

The authors declare that they have no conflict of interest.

Acknowledgements

We acknowledge the Chinese Meridian Project Danzhou GNSS ionospheric TEC product and the auxiliary RINEX geometry record. The Chinese Meridian Project Data Center reprocessed and released the historical GPStation6 observations with the updated product algorithm; Yusen Tian was the responsible data producer. We thank the Chinese Meridian Project (CSTR 31122.02.MSP; https://www.meridianproject.ac.cn/) and its staff for data services and technical support. OpenAI ChatGPT and Codex assisted with language editing, manuscript restructuring, and code-supported consistency checks during revision. The authors reviewed the scientific interpretations, numerical results, citations, and final wording and take responsibility for the manuscript.

Financial support

This research was supported by the Youth Innovation Promotion Association, Chinese Academy of Sciences (2023000116); the National Key R&D Program of China (2025YFF0510703); the Strategic Priority Research Program of the Chinese Academy of Sciences (XDA0470301); and the Specialized Research Fund for the State Key Laboratory of Solar Activity and Space Weather.

References

Alken, P., Thébault, E., Beggan, C. D., Amit, H., Aubert, J., Baerenzung, J., Bondar, T. N., Brown, W. J., Califf, S., Chambodut, A., Chulliat, A., Cox, G. A., Finlay, C. C., Fournier, A., Gillet, N., Grayver, A., Hammer, M. D., Holschneider, M., Huder, L., Hulot, G., Jager, T., Kloss, C., Korte, M., Kuang, W., Kuvshinov, A., Langlais, B., Léger, J.-M., Lesur, V., Livermore, P. W., Lowes, F. J., Macmillan, S., Magnes, W., Mandea, M., Marsal, S., Matzka, J., Metman, M. C., Minami, T., Morschhauser, A., Mound, J. E., Nair, M., Nakano, S., Olsen, N., Pavón-Carrasco, F. J., Petrov, V. G., Ropp, G., Rother, M., Sabaka, T. J., Sanchez, S., Saturnino, D., Schnepf, N. R., Shen, X., Stolle, C., Tangborn, A., Tøffner-Clausen, L., Toh, H., Torta, J. M., Varner, J., Vervelidou, F., Vigneron, P., Wardinski, I., Wicht, J., Woods, A., Yang, Y., Zeren, Z., and Zhou, B.: International Geomagnetic Reference Field: the thirteenth generation, Earth Planets Space, 73, 49, https://doi.org/10.1186/s40623-020-01288-x, 2021.

Balan, N., Liu, L., and Le, H.: A brief review of equatorial ionization anomaly and ionospheric irregularities, Earth Planet. Phys., 2, 257-275, https://doi.org/10.26464/epp2018025, 2018.

Bolmgren, K., Mitchell, C., Bruno, J., and Bust, G.: Tomographic imaging of traveling ionospheric disturbances using GNSS and geostationary satellite observations, J. Geophys. Res.-Space, 125, e2019JA027551, https://doi.org/10.1029/2019JA027551, 2020.

Cheng, P.-H., Lin, C., Otsuka, Y., Liu, H., Rajesh, P. K., Chen, C.-H., Lin, J.-T., and Chang, M.-T.: Statistical study of medium-scale traveling ionospheric disturbances in low-latitude ionosphere using an automatic algorithm, Earth, Planets and Space, 73, 105, https://doi.org/10.1186/s40623-021-01432-1, 2021.

Ding, F., Wan, W., Xu, G., Yu, T., Yang, G., and Wang, J.: Climatology of medium-scale traveling ionospheric disturbances observed by a GPS network in central China, J. Geophys. Res.-Space, 116, A09327, https://doi.org/10.1029/2011JA016545, 2011.

Dunn, C., Meng, X., and Verkhoglyadova, O. P.: Temporal variability of equatorial ionization anomaly crest locations extracted from global ionospheric maps, Space Weather, 22, e2023SW003737, https://doi.org/10.1029/2023SW003737, 2024.

Guerra, M., Cesaroni, C., Ravanelli, M., and Spogli, L.: Travelling ionospheric disturbances detection: A statistical study of detrending techniques, induced period error and near real-time observables, J. Space Weather Space Clim., 14, 17, https://doi.org/10.1051/swsc/2024017, 2024.

Hu, L., Lei, J., Sun, W., Zhao, X., Wu, B., Xie, H., Yang, S., Wu, Z., Zheng, J., Ning, B., Ding, F., and Li, G.: Latitudinal variations of daytime periodic ionospheric disturbances from BeiDou GEO TEC observations over China, J. Geophys. Res.-Space, 126, e2020JA028809, https://doi.org/10.1029/2020JA028809, 2021.

Huang, F., Lei, J., Dou, X., Luan, X., and Zhong, J.: Nighttime medium-scale traveling ionospheric disturbances from airglow imager and Global Navigation Satellite Systems observations, Geophys. Res. Lett., 45, 31-38, https://doi.org/10.1002/2017GL076408, 2018.

Kotake, N., Otsuka, Y., Tsugawa, T., Ogawa, T., and Saito, A.: Climatological study of GPS total electron content variations caused by medium-scale traveling ionospheric disturbances, J. Geophys. Res.-Space, 111, A04306, https://doi.org/10.1029/2005JA011418, 2006.

Le, X., Ren, X., Mei, D., Liu, H., and Zhang, X.: Occurrence and characteristics of medium-scale traveling ionospheric disturbances observed by BeiDou GEO satellites over Hong Kong, J. Geophys. Res.-Space, 129, e2024JA032510, https://doi.org/10.1029/2024JA032510, 2024.

Li, K., Zhang, D., Tian, Y., Sun, S., Gao, H., Zeng, Y., Yang, G., and Hao, Y.: Statistical study on the connections between TEC periodic disturbances associated with MSTIDs and mid-latitude frequency spread F in summer nights over China, J. Geophys. Res.-Space, 130, e2025JA033706, https://doi.org/10.1029/2025JA033706, 2025.

Li, K., Zhang, D., Zeng, Y., Tian, Y., Yang, G., and Hao, Y.: Morphology and climatology of nighttime periodic ionospheric TEC disturbances associated with MSTIDs over China, Space Weather, 22, e2024SW004041, https://doi.org/10.1029/2024SW004041, 2024.

Luo, J., Xu, J., Wu, K., and Sheng, Z.: Investigation on chasing and interaction of traveling ionospheric disturbances based on multi-instrument, J. Geophys. Res.-Space, 129, e2023JA032283, https://doi.org/10.1029/2023JA032283, 2024.

National Space Science Center, Chinese Academy of Sciences (NSSC): Ionospheric Vertical Absolute TEC of GNSS Ionospheric TEC and Scintillation Monitor at Danzhou Station (Version V1.0), National Space Science Data Center [data set], https://doi.org/10.12176/01.06.00588-V01, 2026a.

National Space Science Center, Chinese Academy of Sciences (NSSC): RINEX Format Parameters of GNSS Ionospheric TEC and Scintillation Monitor at Danzhou Station (Version V1.0), National Space Science Data Center [data set], https://doi.org/10.12176/01.06.00578-V01, 2026b.

Nigussie, M., Jakowski, N., and Hoque, M.: Characterization and climatological modeling of equatorial ionization anomaly (EIA) crest position, J. Geophys. Res.-Space, 127, e2022JA030798, https://doi.org/10.1029/2022JA030798, 2022.

Osei-Poku, L., Tang, L., Chen, W., and Chen, M.: Evaluating total electron content (TEC) detrending techniques in determining ionospheric disturbances during lightning events in a low latitude region, Remote Sens., 13, 4753, https://doi.org/10.3390/rs13234753, 2021.

Otsuka, Y., Shinbori, A., Tsugawa, T., and Nishioka, M.: Solar activity dependence of medium-scale traveling ionospheric disturbances using GPS receivers in Japan, Earth, Planets and Space, 73, 22, https://doi.org/10.1186/s40623-020-01353-5, 2021.

Papitashvili, N. E. and King, J. H.: OMNI Hourly Data Set, NASA Space Physics Data Facility [data set], https://doi.org/10.48322/1shr-ht18, 2020.

Saito, A., Fukao, S., and Miyazaki, S.: High resolution mapping of TEC perturbations with the GSI GPS Network over Japan, Geophys. Res. Lett., 25, 3079-3082, https://doi.org/10.1029/98GL52361, 1998.

Shi, J. K., Wang, G. J., Reinisch, B. W., Shang, S. P., Wang, X., Zherebotsov, G., and Potekhin, A.: Relationship between strong range spread F and ionospheric scintillations observed in Hainan from 2003 to 2007, J. Geophys. Res.-Space, 116, A08306, https://doi.org/10.1029/2011JA016806, 2011.

https://doi.org/10.5194/egusphere-2026-5242
Preprint. Discussion started: 14 September 2026

Sun, L., Xu, J., Wang, W., Yuan, W., Li, Q., and Jiang, C.: A statistical analysis of equatorial plasma bubble structures based on an all-sky airglow imager network in China, J. Geophys. Res.-Space, 121, 11495-11517, https://doi.org/10.1002/2016JA022950, 2016.

Tsugawa, T., Otsuka, Y., Coster, A. J., and Saito, A.: Medium-scale traveling ionospheric disturbances detected with dense and wide TEC maps over North America, Geophys. Res. Lett., 34, L22101, https://doi.org/10.1029/2007GL031663, 2007.

Wang, G. J., Shi, J. K., Wang, X., Shang, S. P., Zherebtsov, G., and Pirog, O. M.: The statistical properties of spread F observed at Hainan station during the declining period of the 23rd solar cycle, Ann. Geophys., 28, 1263-1271, https://doi.org/10.5194/angeo-28-1263-2010, 2010.

Wang, Z. and Tian, Y.: Figure source data and derived statistics for seasonal reorganization and near-midnight localization of short-timescale TEC variability over low-latitude Hainan, version 1.0.0, Science Data Bank [data set], https://doi.org/10.57760/sciencedb.00zln, 2026.

Wu, Y. W., Liu, R. Y., Zhang, B. C., Wu, Z. S., Ping, J. S., Liu, J. M., and Hu, Z. J.: Variations of the ionospheric TEC using simultaneous measurements from the China Crustal Movement Observation Network, Ann. Geophys., 30, 1423-1433, https://doi.org/10.5194/angeo-30-1423-2012, 2012.

Xiang, Y., and Gao, Y.: An enhanced mapping function with ionospheric varying height, Remote Sens., 11, 1497, https://doi.org/10.3390/rs11121497, 2019.

Zhang, S.-R., Liu, J., Coster, A. J., Derghazarian, S., Erickson, P. J., Goncharenko, L. P., Aponte, N., and Rideout, W.: Global GNSS observation of mesoscale ionospheric irregularities (2006-2024), J. Geophys. Res.-Space, 131, e2025JA034951, https://doi.org/10.1029/2025JA034951, 2026.

Zhao, B., Wan, W., Liu, L., and Ren, Z.: Characteristics of the ionospheric total electron content of the equatorial ionization anomaly in the Asian-Australian region during 1996-2004, Ann. Geophys., 27, 3861-3873, https://doi.org/10.5194/angeo-27-3861-2009, 2009.